

Article

# Structural Changes of Highly Active Pd/MeO<sub>x</sub> (Me = Fe, Co, Ni) during Catalytic Methane Combustion

Dominik Seeburg<sup>1</sup>, Dongjing Liu<sup>1,2</sup>, Joerg Radnik<sup>1,3</sup> , Hanan Atia<sup>1</sup>, Marga-Martina Pohl<sup>1</sup>, Matthias Schneider<sup>1</sup>, Andreas Martin<sup>1</sup> and Sebastian Wohlrab<sup>1,\*</sup>

<sup>1</sup> Leibniz Institute for Catalysis at the University of Rostock, Albert-Einstein-Str. 29a, D-18059 Rostock, Germany; dominik.seeburg@catalysis.de (D.S.); liudongjing19@163.com (D.L.); joerg.radnik@bam.de (J.R.); hanan.atia@catalysis.de (H.A.); marga-martina.pohl@catalysis.de (M.-M.P.); m.schneider51@gmx.de (M.S.); a.martin.1955@gmx.de (A.M.)

<sup>2</sup> School of Energy and Power Engineering, Jiangsu University, Xuefu Str. 301, Zhenjiang 212013, China

<sup>3</sup> Federal Institute of Materials Testing and Research (BAM), Unter den Eichen 44-46, D-12203 Berlin, Germany

\* Correspondence: sebastian.wohlrab@catalysis.de; Tel.: +49-381-1281-328

Received: 15 December 2017; Accepted: 19 January 2018; Published: 23 January 2018

**Abstract:** Fe<sub>2</sub>O<sub>3</sub>, Co<sub>3</sub>O<sub>4</sub> and NiO nanoparticles were prepared via a citrate method and further functionalized with Pd by impregnation. The pure oxides as well as Pd/Fe<sub>2</sub>O<sub>3</sub>, Pd/Co<sub>3</sub>O<sub>4</sub>, and Pd/NiO (1, 5 and 10 wt % Pd) were employed for catalytic methane combustion under methane lean (1 vol %)/oxygen rich (18 vol %, balanced with nitrogen) conditions. Already, the pure metal oxides showed a high catalytic activity leading to complete conversion temperature of T<sub>100</sub> ≤ 500 °C. H<sub>2</sub>-TPR (Temperature-programmed reduction) experiments revealed that Pd-functionalized metal oxides exhibited enhanced redox activity compared to the pure oxides leading to improved catalytic combustion activity at lower temperatures. At a loading of 1 wt % Pd, 1Pd/Co<sub>3</sub>O<sub>4</sub> (T<sub>100</sub> = 360 °C) outperforms 1Pd/Fe<sub>2</sub>O<sub>3</sub> (T<sub>100</sub> = 410 °C) as well as 1Pd/NiO (T<sub>100</sub> = 380 °C). At a loading of 10 wt % Pd, T<sub>100</sub> could only be slightly reduced in all cases. 1Pd/Co<sub>3</sub>O<sub>4</sub> and 1Pd/NiO show reasonable stability over 70 h on stream at T<sub>100</sub>. XPS (X-ray photoelectron spectroscopy) and STEM (Scanning transmission electron microscopy) investigations revealed strong interactions between Pd and NiO as well as Co<sub>3</sub>O<sub>4</sub>, respectively, leading to dynamic transformations and reoxidation of Pd due to solid state reactions, which leads to the high long-term stability.

**Keywords:** methane total oxidation; methane slip; methane removal; carbon dioxide; combustion

## 1. Introduction

Nowadays, methane is being considered as a renewable energy carrier [1]. However, it is a questionable development since methane possesses a 25 times higher greenhouse gas potential [2], and low temperature exhaust gas streams from combustion engines contain up to 5000 ppm of unburned methane [3]. Hence, the reduction of methane emissions is addressed to novel catalysts, which are highly active at low temperature over time on stream. However, such catalysts are still not yet available.

Pure oxide catalysts, like perovskites [4], are ineligible due to their high temperature demand. It is well known that palladium or platinum are the most efficient active components for the complete oxidation of methane at lower temperature [5]. Particularly, redox active metal oxides can enhance the catalytic performance of Pd active sites via a Mars–van-Krevelen mechanism [6,7]. Redox active supports increase the activity of Pd and provide an enhanced stability on stream [8–11]. Moreover, nanoscale catalysts offer a higher interface and more efficiency for the exhaust gas catalysis [12].

The catalytic activity of Pd is size dependent and increases with increasing particle size due to weakening of the Pd-O bonding [13]. Hoffmann et al. found that a retained redox activity of surface CeO<sub>2</sub> can further enhance the catalytic activity and stability [14]; however, at T<sub>100</sub>, slight activity loss over the first hours on stream was observed.

Huge differences in methane activation abilities have been observed for Pd functionalized Fe, Co and Ni oxides. The reported temperatures of complete combustion differ tremendously by several hundred degrees centigrade, e.g., T<sub>100</sub> = 365 °C for (1 wt %) Pd/Co<sub>3</sub>O<sub>4</sub> [15], T<sub>100</sub> = 540 °C for (1 wt %) Pd/NiO [16] and T<sub>100</sub> = 700 °C for (1 wt %) Pd/Fe<sub>2</sub>O<sub>3</sub> [16]. Out of the iron group elements, only Co based oxide catalysts were described in literature efficient enough for low temperature methane combustion [17–25]. Moreover, Pd/Co<sub>3</sub>O<sub>4</sub> coatings on open cell foams already demonstrated a realistic application potential [26].

In this work, we show that a citrate based synthesis method for Fe<sub>2</sub>O<sub>3</sub>, Co<sub>3</sub>O<sub>4</sub> and NiO nanoparticles as well as a targeted Pd deposition onto these oxides leads to convergence of the methane dry combustion performance for all these catalysts. Moreover, strong interactions between Pd and NiO as well as Pd and Co<sub>3</sub>O<sub>4</sub> were recorded over time, leading to a change of the nature of the active sites, which is discussed according to XPS (X-ray photoelectron spectroscopy) and TEM (Transmission electron microscopy) data.

## 2. Results and Discussion

### 2.1. Catalytic Performance in Methane Combustion

The three oxides, Fe<sub>2</sub>O<sub>3</sub>, Co<sub>3</sub>O<sub>4</sub> and NiO, were prepared from their nitrate precursors under comparable conditions using a citrate method followed by impregnation with a Pd(NO<sub>3</sub>)<sub>2</sub>·2H<sub>2</sub>O aqueous solution to obtain 1, 5 and 10 wt % Pd loading. Figure 1 shows the catalytic combustion of 1 vol % methane in mixture with 18 vol % O<sub>2</sub> and 81 vol % N<sub>2</sub> over the pure oxides as well as over the 1Pd/MeO<sub>x</sub> (1 wt % Pd) catalysts. In all tests, carbon dioxide was the only carbonaceous product.

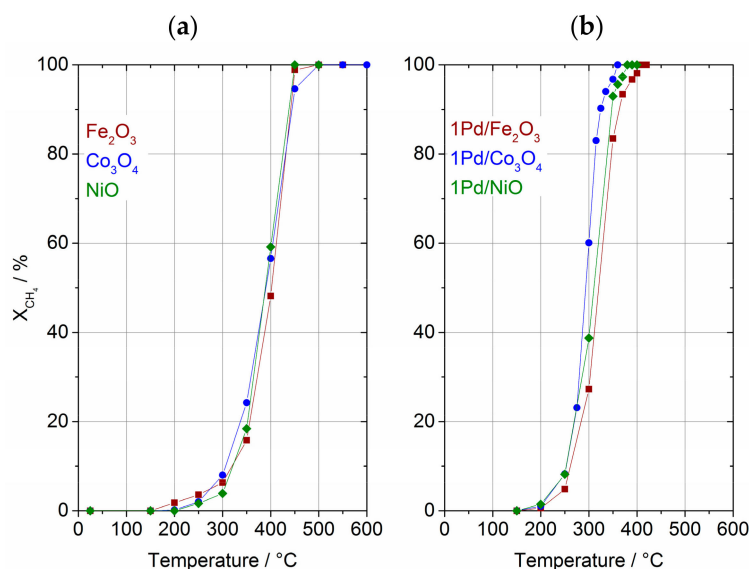


**Figure 1.** Catalytic activity tests for methane combustion, feed gas consisting of CH<sub>4</sub>:O<sub>2</sub>:N<sub>2</sub> = 1:18:81, GHSV (Gas hourly space velocity) = 22,500 L·kg<sup>-1</sup>·h<sup>-1</sup>: (a) Fe<sub>2</sub>O<sub>3</sub>, Co<sub>3</sub>O<sub>4</sub>, NiO (b) 1Pd/Fe<sub>2</sub>O<sub>3</sub>, 1Pd/Co<sub>3</sub>O<sub>4</sub>, 1Pd/NiO.

The light off curves obtained from the reaction over the three pure metal oxide catalysts show nearly the same activity in methane oxidation and reach full conversion at 450 °C in case of NiO and 500 °C in case of Fe<sub>2</sub>O<sub>3</sub>, and Co<sub>3</sub>O<sub>4</sub>, respectively. The combustion temperature decreases of

about 100–150 °C by functionalization of the metal oxides with 1 wt % Pd and full conversion over 1Pd/Co<sub>3</sub>O<sub>4</sub>, 1Pd/NiO, and 1Pd/Fe<sub>2</sub>O<sub>3</sub> is achieved at 360 °C, 380 °C, and 410 °C, respectively (GHSV (Gas hourly space velocity): 22,500 L·kg<sup>-1</sup>·h<sup>-1</sup>, for GHSV variations: see Figure S1). In comparison, Pd supported on Al<sub>2</sub>O<sub>3</sub> performs less efficient due to the inert nature of this kind of support [27–30].

A further decrease in T<sub>100</sub> is possible by functionalization with a higher Pd-content (5 wt % and 10 wt %) as shown in Figure S2. In the case of 5Pd/MeO<sub>x</sub> catalysts, 5Pd/Co<sub>3</sub>O<sub>4</sub> shows the lowest T<sub>100</sub> of 325 °C, 5Pd/Fe<sub>2</sub>O<sub>3</sub> and 5Pd/NiO present a very similar performance with T<sub>100</sub> of about 340 °C. 10Pd/Co<sub>3</sub>O<sub>4</sub> and 10Pd/NiO have nearly the same performance and reach T<sub>100</sub> at 315 °C. In comparison to 5Pd/Fe<sub>2</sub>O<sub>3</sub>, 10Pd/Fe<sub>2</sub>O<sub>3</sub> surprisingly possesses a reduced activity so that a higher T<sub>100</sub> of 365 °C for full CH<sub>4</sub> conversion was reached. However, the slightly increased activity does not justify the higher noble metal contents. Hence, we concentrated our further research to the 1Pd/MeO<sub>x</sub> catalysts.

Figure 2a,b depict long-term tests on stream at ~T<sub>20</sub> and T<sub>100</sub> for the three pure metal oxides (over 50 h) and corresponding 1Pd/MeO<sub>x</sub> catalysts (over 70 h), respectively.

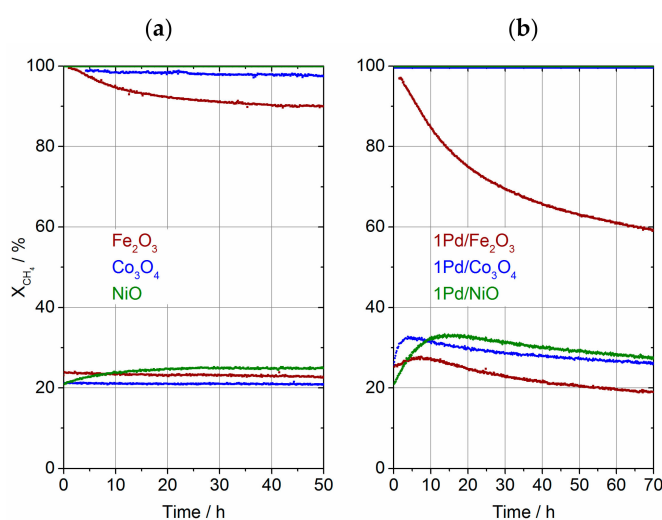


**Figure 2.** Long-term tests at T<sub>20</sub> and T<sub>100</sub>, feed gas consisting of CH<sub>4</sub>:O<sub>2</sub>:N<sub>2</sub> = 1:18:81, GHSV = 22,500 L·kg<sup>-1</sup>·h<sup>-1</sup>: (a) Fe<sub>2</sub>O<sub>3</sub>, Co<sub>3</sub>O<sub>4</sub>, NiO (b) 1Pd/Fe<sub>2</sub>O<sub>3</sub>, 1Pd/Co<sub>3</sub>O<sub>4</sub>, 1Pd/NiO.

The activities of the three pure metal oxides at ~T<sub>20</sub> show reasonable consistency. Fe<sub>2</sub>O<sub>3</sub> and Co<sub>3</sub>O<sub>4</sub> show slight deactivation reflected in methane conversion loss from 23.0 to 22.5% and from 21.0 to 20.8%, respectively. Interestingly, NiO undergoes an activation period seen in an increase in methane conversion from 21.0 to 24.5%. At T<sub>100</sub>, only NiO performs constantly high, whereas Co<sub>3</sub>O<sub>4</sub> and Fe<sub>2</sub>O<sub>3</sub> deactivate to a certain extent. In the case of Co<sub>3</sub>O<sub>4</sub>, a minor loss in methane conversion from 100 to 97% is observed, whereas deactivation is more pronounced for Fe<sub>2</sub>O<sub>3</sub> indicated in a loss in methane conversion from 100 to 91%. All of the corresponding 1Pd/MeO<sub>x</sub> catalysts exhibited an initial activation period at ~T<sub>20</sub> followed by slow deactivation, whereas 1Pd/Fe<sub>2</sub>O<sub>3</sub> is the worst performer. 1Pd/Fe<sub>2</sub>O<sub>3</sub> shows an increase in methane conversion from the start of the experiment from 25.3 to 27.7% after 7.5 h on stream. After reaching a maximum in methane conversion, a slow deactivation takes place and conversion drops down to 19% after 70 h on stream. A better performance was observed using the 1Pd/Co<sub>3</sub>O<sub>4</sub> catalyst. Here, the methane conversion increases from 25.7 to 32.7% after 5 h on stream. Afterwards, the conversion decreases to 26.9% after 70 h on stream. Interestingly, over the 1Pd/NiO catalyst, within 14 h on stream, an increase in conversion from 20.9 to 33.3% is observed, as well as a slow deactivation also occurs after reaching the maximum in methane conversion. Deactivation after 70 h on stream at T<sub>100</sub> was only observed for 1Pd/Fe<sub>2</sub>O<sub>3</sub>, which is reflected in a decrease in methane conversion from 100 to 58%. Importantly, 1Pd/Co<sub>3</sub>O<sub>4</sub> but also 1Pd/NiO perform stable over time at T<sub>100</sub>.

The applicability of these catalysts under exhaust gas conditions, i.e., in the off-gas of a natural gas combustion engine, was simulated and tested. The catalytic activity tests (exhaust gas test—EGT) were performed in a temperature range from 150 to 500 °C with a feed consisting of 0.1 vol % CH<sub>4</sub>, 5.5 vol % CO<sub>2</sub>, 9.0 vol % O<sub>2</sub>, 10.5 vol % H<sub>2</sub>O balanced with N<sub>2</sub> at a modified GHSV of 90,000 L·kg<sup>-1</sup>·h<sup>-1</sup> (Figure 3).

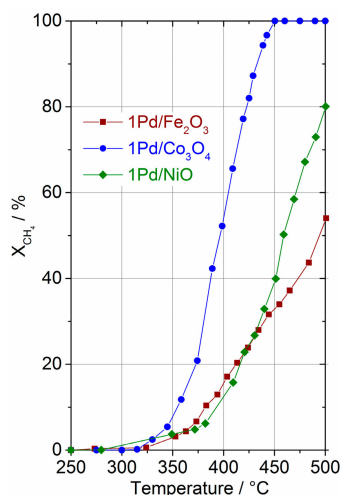


**Figure 3.** Catalytic activity tests under near exhaust gas condition (EGT) with a feed consisting of 0.1 vol % CH<sub>4</sub>, 5.5 vol % CO<sub>2</sub>, 9.0 vol % O<sub>2</sub>, 10.5 vol % H<sub>2</sub>O balanced with N<sub>2</sub> at 90,000 L·kg<sup>-1</sup>·h<sup>-1</sup> for 1Pd/Fe<sub>2</sub>O<sub>3</sub>, 1Pd/Co<sub>3</sub>O<sub>4</sub>, 1Pd/NiO.

Under these conditions the performance of all 1Pd/MeO<sub>x</sub> catalysts is reduced. Accordingly, full conversion was not reached up to 500 °C for Pd/NiO (X<sub>CH<sub>4</sub></sub> = 80%) and Pd/Fe<sub>2</sub>O<sub>3</sub> (X<sub>CH<sub>4</sub></sub> = 54%). Only in case of Pd/Co<sub>3</sub>O<sub>4</sub> complete conversion was recorded at 450 °C (T<sub>100</sub>) and above, which is a quite remarkable result considering occurring water caused deactivation processes at this low temperature in general [31].

## 2.2. Structural Properties and Reducibility of the Catalytic Materials

The obtained specific surface areas of the pure oxides are shown in Table 1. Interestingly, the surface areas of the oxides differ more from each other than their domain sizes. Especially in the case of Co<sub>3</sub>O<sub>4</sub>, the low surface area can be attributed to more intergrown particles compared to Fe<sub>2</sub>O<sub>3</sub>, which reduces the effective surface area. From XRD (X-ray diffraction) investigations, the initial oxide phases were identified as Fe<sub>2</sub>O<sub>3</sub>-hematite (ICSD 088418, [32]), Co<sub>3</sub>O<sub>4</sub> in spinel structure (ICSD 027497, [33]), and NiO in a sodium chloride-like structure (ICSD 043740, [34]) (Figure S3a–c).

**Table 1.** Specific surface areas, Pd-content and MeO<sub>x</sub> crystallite sizes.

Material	S <sub>BET</sub> <sup>1</sup> /m <sup>2</sup> g <sup>-1</sup>	Pd <sup>2</sup> /wt %	Crystallite Size <sup>3</sup> /nm
Fe <sub>2</sub> O <sub>3</sub>	18.7		49 (60)
1Pd/Fe <sub>2</sub> O <sub>3</sub>		1.07	52 (61)
Co <sub>3</sub> O <sub>4</sub>	2.22		63 (63)
1Pd/Co <sub>3</sub> O <sub>4</sub>		0.85	55 (63)
NiO	5.25		40 (52)
1Pd/NiO		0.98	38 (48)

<sup>1</sup> derived from Krypton sorption measurements using the BET (Brunauer–Emmett–Teller) method; <sup>2</sup> from ICP-OES (Inductively Coupled Plasma—Optical Emission Spectrometry) data; <sup>3</sup> calculated from the Scherrer equation at representative Fe<sub>2</sub>O<sub>3</sub> (012), Co<sub>3</sub>O<sub>4</sub> (220) and NiO (111) reflections calculating with the full width half maximum, numbers in brackets are calculated from the reflection area.

Pd crystalline phases were not detectable in 1Pd/MeO<sub>x</sub> catalysts because of the minor metal content and signal broadening of present Pd nanocrystals (see below). The crystallite domain sizes were estimated based on the Scherrer Equation [35] at the (012) reflection of Fe<sub>2</sub>O<sub>3</sub>, the (220) reflection of Co<sub>3</sub>O<sub>4</sub> and the (111) reflection of NiO and are given in Table 1. No significant change of the metal oxide domain size was observed after impregnation with the Pd precursor and subsequent calcination. The determined Pd loading was in the range of the targeted values (~1 wt %) for all Pd-functionalized metal oxides.

H<sub>2</sub>-reduction of the pure MeO<sub>x</sub> as well as the 1Pd/MeO<sub>x</sub> was performed and the specific consumption of hydrogen over temperature is shown in Figure 4. The formation of intermediate phases and their transformation was detected with in situ XRD measurements (Figures S4–S6) showing that the reduction of the pure metal oxides starts at ca. 300 °C in all cases.

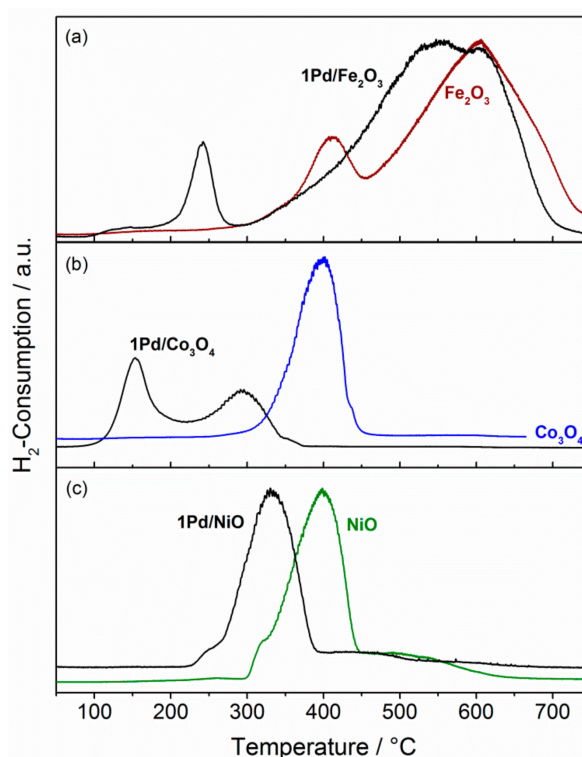


**Figure 4.** H<sub>2</sub>-TPR (Temperature-programmed reduction) profiles of (a) Fe<sub>2</sub>O<sub>3</sub> and 1Pd/Fe<sub>2</sub>O<sub>3</sub> (b) Co<sub>3</sub>O<sub>4</sub> and 1Pd/Co<sub>3</sub>O<sub>4</sub>, (c) NiO and 1Pd/NiO.

The reduction of Co<sub>3</sub>O<sub>4</sub> completed at ca. 450 °C and Co metal was detected. For NiO and Fe<sub>2</sub>O<sub>3</sub>, the required temperatures are remarkably higher at 600 °C and 750 °C, respectively. Only in the case of the iron oxide does an intermediate phase appear and Fe<sub>3</sub>O<sub>4</sub> is obtained at ca. 400 °C, which is further reduced to metallic Fe with increasing temperature. In all cases, Pd functionalization decreases the reduction temperature in comparison to the pure metal oxides, presumably, by hydrogen spillover from the Pd to the supports and subsequent reduction of the metal oxides [36]. Additional intermediates appear only in the case of Pd/Co<sub>3</sub>O<sub>4</sub> reduction as CoO at around 300 °C, which is subsequently reduced to Co. Generally, the reducibility with H<sub>2</sub> is a good measure to roughly evaluate the redox activity, which can be classified in the following order: 1Pd/Co<sub>3</sub>O<sub>4</sub> >> 1Pd/Fe<sub>2</sub>O<sub>3</sub> > 1Pd/NiO (with onset temperatures of 100 °C, 200 °C, 220 °C, respectively). Since all 1Pd/MeO<sub>x</sub> catalysts do not differ much under dry oxidation conditions, these differences could help to explain the different activities in the exhaust gas tests. Ciuparu and co-workers found that high oxygen mobility in oxides leads to stronger resistance against water caused deactivation [37]. From the H<sub>2</sub>-TPR results, we can assume that surface oxygen activation on 1Pd/Co<sub>3</sub>O<sub>4</sub> occurs at much lower temperature than on the other



catalysts. This behaviour could be reflected in the catalytic methane oxidation under simulated exhaust gas conditions (Figure 3).

HAADF-STEM (High-angle annular dark-field scanning transmission electron microscopy) images of fresh 1Pd/MeO<sub>x</sub> (Figure 5) show that Pd (PdO) particles (bright particles) of ca. 2–8 nm are randomly distributed over all the metal oxides. The Pd particles have irregular morphologies with compact height. Particle sizes of MeO<sub>x</sub> (Me = Fe, Co, Ni) detected via STEM are in accordance to crystallite domain sizes determined from XRD (Scherrer method).

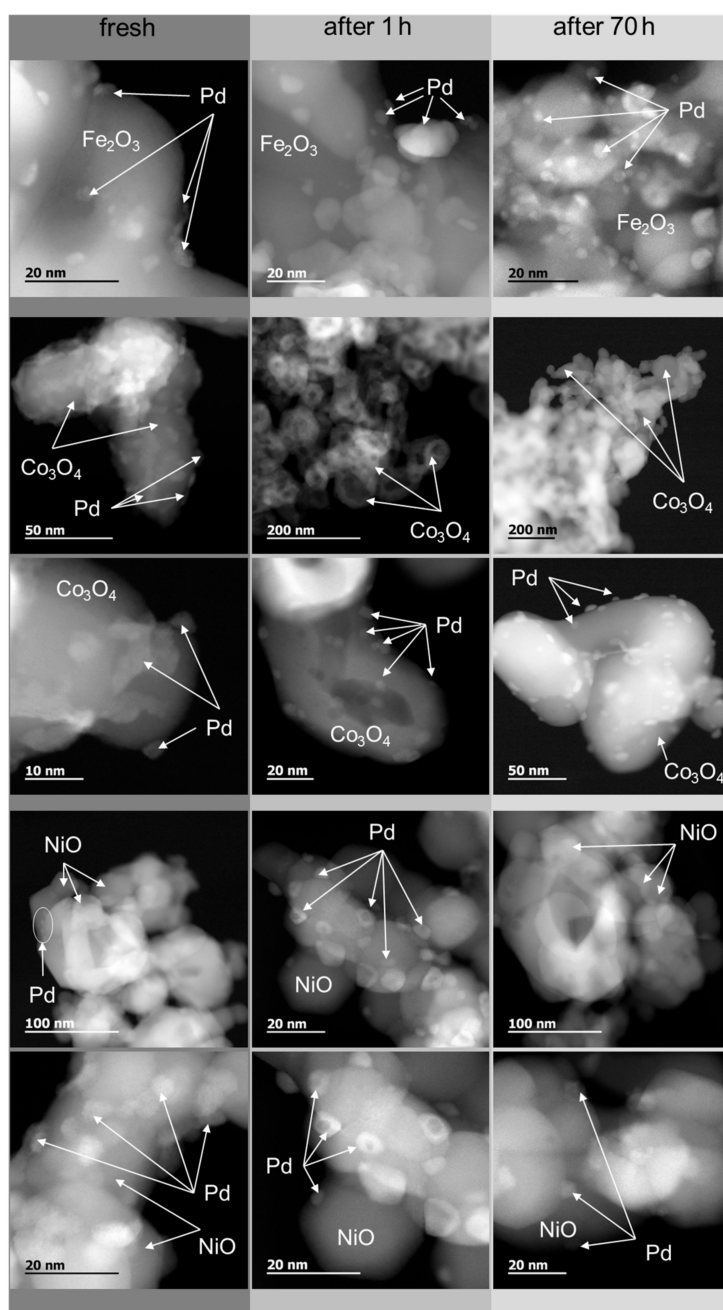


**Figure 5.** HAADF-STEM (High-angle annular dark-field scanning transmission electron microscopy) images of fresh and spent samples after long-term tests (at  $T_{100}$ , feed gas consisting of  $\text{CH}_4:\text{O}_2:\text{N}_2 = 1:18:81$ , at  $22,500 \text{ L}\cdot\text{kg}^{-1}\cdot\text{h}^{-1}$ ): 1Pd/Fe<sub>2</sub>O<sub>3</sub>, 1Pd/Co<sub>3</sub>O<sub>4</sub> and 1Pd/NiO.

### 2.3. Catalyst Transformation during Time on Stream

Spent 1Pd/MeO<sub>x</sub> catalysts were examined via transmission electron microscopy (Figure 5 and Figures S7, S13 and S16). In addition, 1Pd/Co<sub>3</sub>O<sub>4</sub> and 1Pd/NiO showed a changed morphology after being used on stream. In the case of 1Pd/Co<sub>3</sub>O<sub>4</sub>, a sponge-like structure gets visible after 1 h on stream (Figure S12), whereas, after 70 h, the catalyst seems to be restructured. In the case of 1Pd/NiO, holes in the Pd particles are formed and a flat surface coverage of Pd on the NiO surface can be detected after 70 h on stream. Since the Pd phase is located at an oxidic support, EDX (Energy-dispersive X-ray spectroscopy) does not help to reveal the oxidation state of the Pd. When analysing the oxidation states of the Pd particles via FFT (fast Fourier transform), we found mostly PdO in the fresh catalysts, Pd or Pd suboxides in the catalysts after 1 h on stream, and reoxidation to PdO in the catalysts after 1 h on stream (FFT of the high resolution images (see Figures S8–S11, S14, S15, S17 and S18)). However, these investigations are single shots on some particles. Although they show that Pd is present in different oxidation states, a method describing the whole sample was required.

In order to understand the dynamic processes to their full extent, XPS spectra of fresh and spent (after 1 h and 70 h on stream and after tests with simulated exhaust gas) 1Pd/MeO<sub>x</sub> were recorded and presented in Figure 6. For all three 1Pd/MeO<sub>x</sub> catalysts at the different reaction stages, no significant change in Fe, Co and Ni spectra was observed, which indicates no change in metal oxide phase (Figures S19–S21).

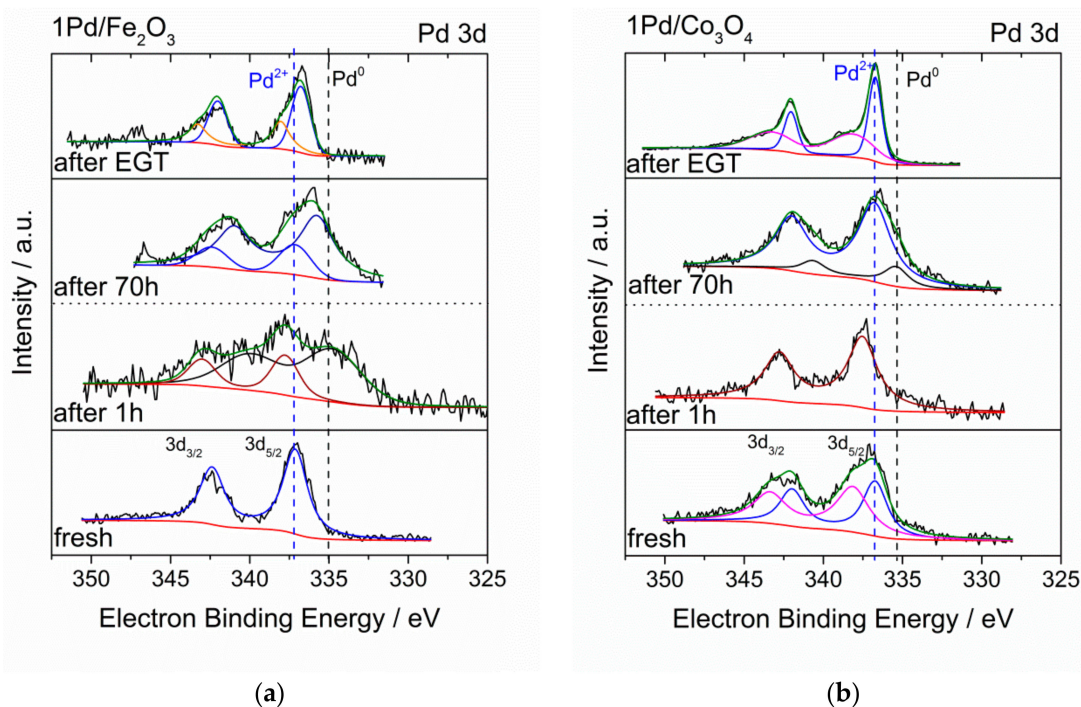
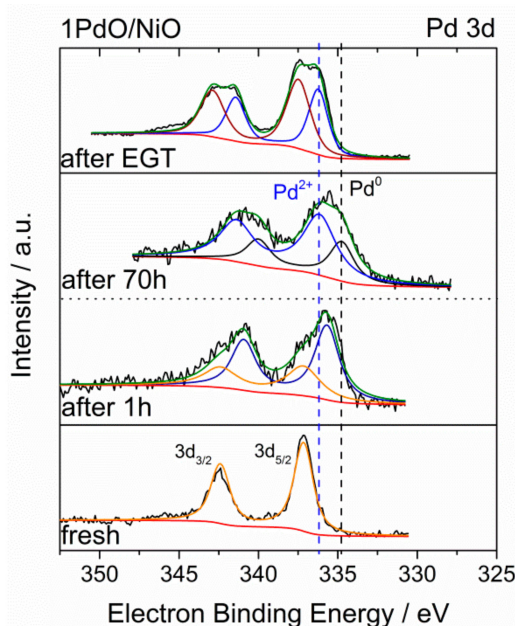


Figure 6. Cont.



(c)

**Figure 6.** XPS (X-ray photoelectron spectroscopy) spectra of Pd 3d electrons of fresh and spent Pd/MeO<sub>x</sub> after long-term tests at T<sub>100</sub> (feed gas consisting of CH<sub>4</sub>:O<sub>2</sub>:N<sub>2</sub> = 1:18:81, at 22,500 L·kg<sup>-1</sup>·h<sup>-1</sup>) as well as after being used for exhaust gas treatment (feed consisting of 0.1 vol % CH<sub>4</sub>, 5.5 vol % CO<sub>2</sub>, 9.0 vol % O<sub>2</sub>, 10.5 vol % H<sub>2</sub>O balanced in N<sub>2</sub> at 90,000 L·kg<sup>-1</sup>·h<sup>-1</sup>): (a) 1Pd/Fe<sub>2</sub>O<sub>3</sub>, (b) 1Pd/Co<sub>3</sub>O<sub>4</sub> and (c) 1Pd/NiO.

Typical Pd<sup>2+</sup> peaks at ca. 336.7 eV [38] are detected in all the fresh 1Pd/MeO<sub>x</sub>. After 1 h on stream at T<sub>100</sub>, for all 1Pd/MeO<sub>x</sub> catalysts, changes in the oxidation state of Pd were found. In the case of 1Pd/Fe<sub>2</sub>O<sub>3</sub> and 1Pd/NiO, an increasing amount of metallic Pd was observed. Contrary, PdO was the dominant Pd-species in 1Pd/Co<sub>3</sub>O<sub>4</sub>. After 70 h on stream at T<sub>100</sub>, the amount of PdO in 1Pd/Co<sub>3</sub>O<sub>4</sub> is still high as well as that of 1Pd/NiO increased. In 1Pd/Fe<sub>2</sub>O<sub>3</sub>, the highest amount of metallic Pd was found. Moreover, in Pd/Co<sub>3</sub>O<sub>4</sub> and Pd/NiO, a peak with an electron binding energy at around 336 eV can be observed, which can be correlated to Pd suboxides. In summary, on Fe<sub>2</sub>O<sub>3</sub>, metallic Pd dominates after the long-term tests, whereas oxidic Pd is more present on NiO and, especially, on Co<sub>3</sub>O<sub>4</sub>. The reducibility of Pd depends on the support in the order Fe<sub>2</sub>O<sub>3</sub> > NiO > Co<sub>3</sub>O<sub>4</sub>.

In correlation to the catalytic results, 1Pd/Fe<sub>2</sub>O<sub>3</sub> shows a good initial performance in methane combustion, but, in the long-term test over 70 h at T<sub>100</sub>, deactivation is observed. This behaviour probably attributes to the lower oxidation potential of the Fe<sub>2</sub>O<sub>3</sub> particles to form sufficient content of PdO, which is necessary for methane oxidation. A better performance is observed for 1Pd/NiO. It remains stable without any deactivation until the end of the long-term test at T<sub>100</sub>, possibly due to restructuring accompanied by reoxidation. This process obviously is driven by the nanoscale Kirkendall effect [39,40] between Pd and NiO during the catalytic methane combustion. 1Pd/Co<sub>3</sub>O<sub>4</sub> possesses the lowest T<sub>100</sub> and, in the long-term test at T<sub>100</sub>, also no deactivation is observed. Strong interactions between Pd and Co<sub>3</sub>O<sub>4</sub> at the metal oxide interface lead to continuously newly formed active species at the catalyst surface.

After catalytic tests with a simulated exhaust gas (EGT), all spent 1Pd/MeO<sub>x</sub> contained two Pd species with higher binding energy. Obviously, water acts as an inhibitor for the catalytic cycle and can be responsible for the lower activity of 1Pd/Fe<sub>2</sub>O<sub>3</sub> and 1Pd/NiO compared to 1Pd/Co<sub>3</sub>O<sub>4</sub>.



### 3. Materials and Experimental Details

#### 3.1. Catalyst Preparation

Fe<sub>2</sub>O<sub>3</sub>, Co<sub>3</sub>O<sub>4</sub> and NiO were prepared reproducibly using a citrate method more than three times. First, ethylene glycol (2.48 g, >99%, Carl Roth, Karlsruhe, Germany) was added to a solution of citric acid (57.6 g, >99.5%, Carl Roth, Karlsruhe, Germany) in methanol (150 mL, >99%, Carl Roth, Karlsruhe, Germany). Afterwards, the corresponding metal nitrate (>99.9%, Fluka, Steinheim, Germany) precursors (0.01 mol) were added and esterification from ethylene glycol and metal citrate was performed at 130 °C until 2 h. Subsequently, the solid was treated in vacuum at 180 °C for 2 h. Finally, calcination was performed at 500 °C for 3 h with a heating rate of 2 °C/min. The resulting metal oxides were impregnated by the incipient wetness method with aqueous Pd(NO<sub>3</sub>)<sub>2</sub>·2H<sub>2</sub>O (~40% Pd, Carl Roth, Karlsruhe, Germany) solution (M adjusted to the pore volume) to obtain 1 wt %, 5 wt % and 10 wt % Pd loading reproducibly more than three times, hereinafter denoted as 1Pd/MeO<sub>x</sub> (MeO<sub>x</sub> = Fe<sub>2</sub>O<sub>3</sub>, Co<sub>3</sub>O<sub>4</sub> and NiO), 5Pd/MeO<sub>x</sub> and 10Pd/MeO<sub>x</sub>, respectively. The samples were dried at 80 °C for 12 h and calcined at 400 °C in air (heating rate of 2 °C/min) for 2 h.

#### 3.2. Catalysts Characterization

##### 3.2.1. Kr Corption

The BET specific surface area of the catalysts was measured by Krypton adsorption using an ASAP 2020 instrument from Micromeritics (Norcross, GA, USA). The samples were heated under vacuum for 30 min at 150 °C before the Krypton adsorption isotherms were measured.

##### 3.2.2. X-ray Powder Diffraction (XRD)

XRD profiles were measured using a STADI P transmission diffractometer from STOE (Darmstadt, Germany). The samples were ground and afterwards analysed applying a curved germanium monochromator in the incident beam path, CuK<sub>α</sub> radiation ( $\lambda = 0.15406$  nm) and a 6° linear position sensitive detector (PSD). The crystallite domain sizes were calculated based on the Scherrer equation at representative Fe<sub>2</sub>O<sub>3</sub> (012), Co<sub>3</sub>O<sub>4</sub> (220) and NiO (111) reflections.

##### 3.2.3. Element Analysis

A Varian 715-ES inductively coupled plasma-optical emission spectrometer (ICP-OES) (Palo Alto, CA, USA) was used for the determination of the elemental composition of the catalysts after complete dissolution in a solution containing 8 mL of aqua regia and 2 mL hydrofluoric acid.

##### 3.2.4. In Situ X-ray Diffraction (In Situ XRD)

The in situ XRD reduction experiments were carried out on an X'Pert Pro (Panalytical, Almelo, The Netherlands) with a Material-Research-Instrument-TC-basic (Physikalische Geraete GmbH, Karlsruhe, Germany) high temperature chamber to perform reduction with hydrogen at different temperatures. Furthermore, 30 mg of the respective powders were heated indirectly by an AlCr-sheet. The X-ray diffraction patterns were measured every 50 °C (heating rate 10 °C/min) and the reduction atmosphere consisted of 5 vol % H<sub>2</sub> in He (5.0, Air Liquide Germany, Düsseldorf, Germany), with a total flow rate of 10 mL/min.

##### 3.2.5. Temperature Programmed Hydrogen Reduction (H<sub>2</sub>-TPR)

Prior to the temperature programmed reduction (H<sub>2</sub>-TPR) experiments with 10–20 mg of each sample a preheating for 30 min in air (50 mL/min) to 400 °C was performed. After cooling, the measurement was started. For this purpose, the samples were heated to 700 °C in an H<sub>2</sub>:Ar = 5:95 flow with a temperature ramp of 10 °C/min, the final temperature was kept for 1 h, hydrogen

consumption was monitored by an online thermal conductivity detector (Mircomeritics ChemiSorb 2920-Instrument, Norcross, GA, USA).

### 3.2.6. Scanning Electron Microscopy (SEM)

The SEM measurements were performed at 10.0 kV with a JSM-4701 (JEOL) microscope (Akishima, Tokyo, Japan).

### 3.2.7. Transmission Electron Microscopy (TEM)

The TEM measurements were performed at 200 kV with an aberration-corrected JEM-ARM200F (JEOL, Corrector: CEOS, Tokyo, Japan). The microscope is equipped with a JED-2300 (JEOL) energy-dispersive X-ray-spectrometer (EDXS) (Akishima, Tokyo, Japan). The aberration corrected STEM imaging (High-Angle Annular Dark Field (HAADF) and Annular Bright Field (ABF)) were performed under the following conditions. HAADF and ABF both were done with a spot size of approximately 0.1 nm, a convergence angle of 30–36° and collection semi-angles for HAADF and ABF of 90–170 mrad and 11–22 mrad, respectively. The solid samples were deposited without any pretreatment on a holey carbon supported Cu-grid (mesh 300) and transferred to the microscope.

### 3.2.8. X-ray Photoelectron Spectroscopy (XPS)

X-ray photoelectron spectroscopy (XPS) experiments were performed by a VG ESCALAB 220iXL system (VG Scientific, Waltham, MA, USA) with monochromatic Al-K $\alpha$ -radiation ( $E = 1486.6$  eV). As internal reference, for the electron binding energy, adventitious carbon with a C1s binding energy of 284.8 eV was used. The peaks were fitted with mixed Gaussian–Lorentzian curves after subtracting a Shirley background.

## 3.3. Catalyst Testing for CH<sub>4</sub> Combustion

CH<sub>4</sub> combustion catalytic tests were performed in a vertical fixed-bed plug-flow quartz tubular reactor (inner diameter of 8 mm) at ambient pressure. In addition, 0.2 g of the powder catalyst was placed in the isothermal reactor zone and fixed by quartz wool (>99.9%, Carl Roth, Karlsruhe, Germany) located downstream below the catalyst bed. The catalytic activity was measured starting from 150 °C with a stepwise increase at a temperature of 50 K steps maximum until full conversion of methane was achieved. At each temperature, methane conversion was recorded threefold within 30 min using an online gas chromatograph (Agilent 7890A, Santa Clara, CA, USA) equipped with a methanizer for flame ionization detection and a thermal conductivity detector. The feed components as well as the reaction products were detected, except water. Each experiment of these series was repeated and the deviation of absolute values was always below 2% for each measuring point. In separate experiments, Fe<sub>2</sub>O<sub>3</sub>, Co<sub>3</sub>O<sub>4</sub>, NiO as well as 1Pd/Fe<sub>2</sub>O<sub>3</sub>, 1Pd/Co<sub>3</sub>O<sub>4</sub>, 1Pd/NiO were tested under isothermal conditions at T<sub>20</sub>, T<sub>100</sub> (the specific temperatures necessary for 20 or 100% methane conversion, respectively) over 50 or 70 h on stream. In all tests, the reactant gas stream consisted of methane (2.5, Air Liquide Germany, Düsseldorf, Germany), oxygen (5.0, Linde, Pullach, Germany) and nitrogen (5.0, Linde, Pullach, Germany) in the ratio of 1:18:81 representing a feed of 1.0 vol % CH<sub>4</sub>. The gas flows were controlled with mass flow controllers supplied from MKS Instruments (Andover, MA, USA). The total flow rate was 75 cm<sup>3</sup>·min<sup>-1</sup> corresponding to ~22,500 L·kg<sup>-1</sup>·h<sup>-1</sup>.

The light off tests with simulated exhaust gas were performed in a temperature range from 150–500 °C with a heating rate of about 2 °C·min<sup>-1</sup>. The temperature was controlled with a thermocouple inside of a quartz capillary in the middle of the catalyst bed. At 500 °C, the reaction was performed for 1 h; afterwards, the reaction temperature was decreased to 460 °C, 430 °C, 410 °C, 390 °C, 370 °C, 360 °C, and 150 °C; at each temperature, the catalytic performance was measured for 30 min, with a feed consisting of 0.1 vol % CH<sub>4</sub>, 5.5 vol % CO<sub>2</sub> (4.5, Linde, Pullach, Germany), 9.0 vol % O<sub>2</sub>, 10.5 vol % H<sub>2</sub>O (LC-MS-Grade, Carl Roth, Karlsruhe, Germany) balanced with N<sub>2</sub> at a total flow of about 300 cm<sup>3</sup>·mL<sup>-1</sup> corresponding to a modified GHSV of 90,000 L·kg<sup>-1</sup>·h<sup>-1</sup>.

The gas flows were controlled with mass flow controllers supplied from MKS Instruments (Andover, MA, USA). Admixing of liquid water was controlled by a mini-Cori-Flow mass flow controller (Bronkhorst High-Tech B.V., Ruurlo, The Netherlands) followed by an evaporation chamber heated to 150 °C in which the gaseous steam was mixed with CH<sub>4</sub>, O<sub>2</sub>, CO<sub>2</sub> and N<sub>2</sub> before the reactor. Product analysis was carried out without any water condensation online at ca. 180 °C by IR spectral analysis and linear combination of bands to fit the measured spectrum using a Gasmeter CX4000 device (Gasmeter Technologies, Helsinki, Finland).

#### 4. Conclusions

Fe<sub>2</sub>O<sub>3</sub>, Co<sub>3</sub>O<sub>4</sub> and NiO prepared via citrate method were functionalized with Pd yielding highly active catalysts for catalytic methane dry combustion. The interactions between metal and support lead to different catalytic properties under humid exhaust gas conditions and can be roughly correlated with reducibility measured by H<sub>2</sub>-TPR. By comparing the XPS and STEM information at different times on stream, we can conclude in greater detail that (i) different Pd oxidation states on stream, accompanied by (ii) a restructuring of the metal-support structure occur. Obviously, strong dynamic interactions between Pd and the metal oxide take place, e.g., in the case of 1Pd/NiO Pd-hollow structures are formed, whereas, in the case of 1Pd/Co<sub>3</sub>O<sub>4</sub>, sponge-like structures of the Co<sub>3</sub>O<sub>4</sub> support are being built. These interactions lead to a restructuring accompanied by reoxidation of active sites, which is the origin of the long-term stability over 70 h on stream for 1Pd/NiO and 1Pd/Co<sub>3</sub>O<sub>4</sub> at T<sub>100</sub>.

**Supplementary Materials:** The following are available online at <http://www.mdpi.com/2073-4344/8/2/42/s1>, Figure S1: Catalytic activity tests for methane combustion, feed gas consisting of CH<sub>4</sub>:O<sub>2</sub>:N<sub>2</sub> = 1:18:81, catalyst masses: 300, 200 and 50 mg, catalysts: 1Pd/Fe<sub>2</sub>O<sub>3</sub>, 1Pd/Co<sub>3</sub>O<sub>4</sub> and 1Pd/NiO. Figure S2: Catalytic activity tests for methane combustion, feed gas consisting of CH<sub>4</sub>:O<sub>2</sub>:N<sub>2</sub> = 1:18:81, at 22,500 L·kg<sup>-1</sup>·h<sup>-1</sup>: (left) 5Pd/Fe<sub>2</sub>O<sub>3</sub>, 5Pd/Co<sub>3</sub>O<sub>4</sub>, 5Pd/NiO (right) 10Pd/Fe<sub>2</sub>O<sub>3</sub>, 10Pd/Co<sub>3</sub>O<sub>4</sub>, 10Pd/NiO. Figure S3: XRD Diffraction patterns of (a) Fe<sub>2</sub>O<sub>3</sub>, 1Pd/Fe<sub>2</sub>O<sub>3</sub>, 5Pd/Fe<sub>2</sub>O<sub>3</sub>, 10Pd/Fe<sub>2</sub>O<sub>3</sub>, (b) Co<sub>3</sub>O<sub>4</sub>, 1Pd/Co<sub>3</sub>O<sub>4</sub>, 5Pd/Co<sub>3</sub>O<sub>4</sub>, 10Pd/Co<sub>3</sub>O<sub>4</sub> and (c) NiO, 1Pd/NiO, 5Pd/NiO, 10Pd/NiO; \* PdO reference (ICSD 24692). Figure S4: In situ XRD under H<sub>2</sub> reduction (a) Fe<sub>2</sub>O<sub>3</sub> and (b) 1Pd/Fe<sub>2</sub>O<sub>3</sub>, 5 vol % H<sub>2</sub> in He, 10 mL·min<sup>-1</sup> with a heating rate of 10 K/min (slightly higher phase transition temperatures are specific for the method). Figure S5: In situ XRD under H<sub>2</sub> reduction (a) Co<sub>3</sub>O<sub>4</sub> and (b) 1Pd/Co<sub>3</sub>O<sub>4</sub>, 5 vol % H<sub>2</sub> in He, 10 mL·min<sup>-1</sup> with a heating rate of 10 K/min (slightly higher phase transition temperatures are specific for the method). Figure S6: In situ XRD under H<sub>2</sub> reduction (a) NiO and (b) 1Pd/NiO, 5 vol % H<sub>2</sub> in He, 10 mL/min with a heating rate of 10 K/min (slightly higher phase transition temperatures are specific for the method). Figure S7: HAADF-STEM images of fresh and spent samples after long-term tests (at T<sub>100</sub>, feed gas consisting of CH<sub>4</sub>:O<sub>2</sub>:N<sub>2</sub> = 1:18:81, at 22,500 L·kg<sup>-1</sup>·h<sup>-1</sup>): 1Pd/Fe<sub>2</sub>O<sub>3</sub>. Figure S8: HAADF-STEM, FFT and inverse FFT of fresh 1Pd/Fe<sub>2</sub>O<sub>3</sub>. Figure S9: HAADF-STEM, FFT and inverse FFT of 1Pd/Fe<sub>2</sub>O<sub>3</sub> after 1 h on stream. Figure S10: HAADF-STEM, FFT and inverse FFT of 1Pd/Fe<sub>2</sub>O<sub>3</sub> after 1 h on stream. Figure S11: HAADF-STEM, FFT and inverse FFT of 1Pd/Fe<sub>2</sub>O<sub>3</sub> after 70 h on stream. Figure S12: SEM images of fresh and spent samples after long-term tests (at T<sub>100</sub>, feed gas consisting of CH<sub>4</sub>:O<sub>2</sub>:N<sub>2</sub> = 1:18:81, at 22,500 L·kg<sup>-1</sup>·h<sup>-1</sup>): 1Pd/Co<sub>3</sub>O<sub>4</sub>. Figure S13: HAADF-STEM images of fresh and spent samples after long-term tests (at T<sub>100</sub>, feed gas consisting of CH<sub>4</sub>:O<sub>2</sub>:N<sub>2</sub> = 1:18:81, at 22,500 L·kg<sup>-1</sup>·h<sup>-1</sup>): 1Pd/Co<sub>3</sub>O<sub>4</sub>. Figure S14: HAADF-STEM, FFT and inverse FFT of 1Pd/Co<sub>3</sub>O<sub>4</sub> after 1 h on stream. Figure S15: HAADF-STEM, FFT and inverse FFT of 1Pd/Co<sub>3</sub>O<sub>4</sub> after 70 h on stream. Figure S16: HAADF-STEM images of fresh and spent samples after long-term tests (at T<sub>100</sub>, feed gas consisting of CH<sub>4</sub>:O<sub>2</sub>:N<sub>2</sub> = 1:18:81, at 22,500 L·kg<sup>-1</sup>·h<sup>-1</sup>): 1Pd/NiO. Figure S17: HAADF-STEM, FFT and inverse FFT of 1Pd/NiO after 1 h on stream. Figure S18: HAADF-STEM, FFT and inverse FFT of 1Pd/NiO after 70 h on stream. Figure S19: 1Pd/Fe<sub>2</sub>O<sub>3</sub>-XPS spectra of fresh and spent samples, after 1 h, 70 h and after test with exhaust gas (EGT). Figure S20: 1Pd/Co<sub>3</sub>O<sub>4</sub>-XPS spectra of fresh and spent samples, after 1 h, 70 h and after test with exhaust gas (EGT). Figure S21: 1Pd/NiO-XPS spectra of fresh and spent samples, after 1 h, 70 h and after test with exhaust gas (EGT).

**Acknowledgments:** This work is partially supported by the CSC (China Scholarship Council) and DAAD (Deutscher Akademischer Austausch Dienst). The authors gratefully acknowledge Ralph Kraehnert (TU Berlin) for SEM analysis. We thank Anja Simmulla for analytical support.

**Author Contributions:** S.W. and A.M. conceived the project. D.S. conceived, designed and performed the experiments; J.R., H.A., M.-M.P. and M.S. characterized the materials (XPS, TPR, TEM and XRD); D.S., D.L., J.R., M.-M.P. and S.W. analyzed the data; and D.S., D.L. and S.W. wrote the paper.

**Conflicts of Interest:** The authors declare no conflict of interest.

## References

1. Götz, M.; Lefebvre, J.; Mörs, F.; McDaniel Koch, A.; Graf, F.; Bajohr, S.; Reimert, R.; Kolb, T. Renewable Power-to-Gas: A technological and economic review. *Renew. Energy* **2016**, *85*, 1371–1390. [[CrossRef](#)]
2. Forster, P.; Ramaswamy, V.; Artaxo, P.; Bernsten, T.; Betts, R.; Fahey, D.W.; Haywood, J.; Lean, J.; Lowe, D.C.; Myhre, G.; et al. Climate Change 2007: The Physical Science Basis. In *Contribution of Working Group I to the Fourth Assessment Report of the Intergovernmental Panel on Climate Change*; Solomon, S., Qin, D., Manning, M., Chen, Z., Marquis, M., Averyt, K.B., Tignor, M., Miller, H.L., Eds.; Cambridge University Press: Cambridge, UK; New York, NY, USA, 2007; p. 212.
3. Zanoletti, M.; Klvana, D.; Kirchnerova, J.; Perrier, M.; Guy, C. Auto-cyclic reactor: Design and evaluation for the removal of unburned methane from emissions of natural gas engines. *Chem. Eng. Sci.* **2009**, *64*, 945–954. [[CrossRef](#)]
4. Ladavos, A.; Pomonis, P. *Methane Combustion on Perovskites in Perovskites and Related Mixed Oxides: Concepts and Applications*; Wiley: Weinheim, Germany, 2016; Volume 2, pp. 369–388.
5. Li, Z.; Hoflund, G.B. A Review on Complete Oxidation of Methane at Low Temperatures. *J. Nat. Gas Chem.* **2003**, *12*, 153–160.
6. Garbowski, E.; Feumi-Jantou, C.; Mouaddib, N.; Primet, M. Catalytic combustion of methane over palladium supported on alumina catalysts: Evidence for reconstruction of particles. *Appl. Catal. A* **1994**, *109*, 277–291. [[CrossRef](#)]
7. Ciuparu, D.; Lyubovsky, M.R.; Altman, E.; Pfefferle, L.D.; Datye, A. Catalytic Combustion of Methane over Palladium-Based Catalysts. *Catal. Rev.* **2002**, *44*, 593–649. [[CrossRef](#)]
8. Escandón, L.S.; Ordóñez, S.; Vega, A.; Díez, F.V. Oxidation of methane over palladium catalysts: Effect of the support. *Chemosphere* **2005**, *58*, 9–17. [[CrossRef](#)] [[PubMed](#)]
9. Van Vegten, N.; Maciejewski, M.; Krumeich, F.; Baiker, A. Structural properties, redox behaviour and methane combustion activity of differently supported flame-made Pd catalysts. *Appl. Catal. B* **2009**, *93*, 38–49. [[CrossRef](#)]
10. Eguchi, K.; Arai, H. Low temperature oxidation of methane over Pd-based catalysts—Effect of support oxide on the combustion activity. *Appl. Catal. A* **2001**, *222*, 359–367. [[CrossRef](#)]
11. Xiao, L.-H.; Sun, K.-P.; Xu, X.-L.; Li, X.-N. Low-temperature catalytic combustion of methane over Pd/CeO<sub>2</sub> prepared by deposition-precipitation method. *Catal. Commun.* **2005**, *6*, 796–801. [[CrossRef](#)]
12. Di Sarli, V.; Landi, G.; Lisi, L.; Saliva, A.; Di Benedetto, A. Catalytic diesel particulate filters with highly dispersed ceria: Effect of the soot-catalyst contact on the regeneration performance. *Appl. Catal. B* **2016**, *197*, 116–124. [[CrossRef](#)]
13. Roth, D.; Gélín, P.; Kaddouri, A.; Garbowski, E.; Primet, M.; Tena, E. Oxidation behaviour and catalytic properties of Pd/Al<sub>2</sub>O<sub>3</sub> catalysts in the total oxidation of methane. *Catal. Today* **2006**, *112*, 134–138. [[CrossRef](#)]
14. Hoffmann, M.; Kreft, S.; Georgi, G.; Fulda, G.; Pohl, M.-M.; Seeburg, D.; Berger-Karin, C.; Kondratenko, E.V.; Wohlrab, S. Improved catalytic methane combustion of Pd/CeO<sub>2</sub> catalysts via porous glass integration. *Appl. Catal. B* **2015**, *179*, 313–320. [[CrossRef](#)]
15. Li, Z.; Hoflund, G.B. Catalytic oxidation of methane over Pd/Co<sub>3</sub>O<sub>4</sub>. *React. Kinet. Catal. Lett.* **1999**, *66*, 367–374. [[CrossRef](#)]
16. Ishihara, T.; Shigematsu, H.; Abe, Y.; Takita, Y. Effects of Additives on the Activity of Palladium Catalysts for Methane Combustion. *Chem. Lett.* **1993**, *22*, 407–410. [[CrossRef](#)]
17. Chen, J.; Zhang, X.; Arandiyani, H.; Peng, Y.; Chang, H.; Li, J. Low temperature complete combustion of methane over cobalt chromium oxides catalysts. *Catal. Today* **2013**, *201*, 12–18. [[CrossRef](#)]
18. Ercolino, G.; Grzybek, G.; Stelmachowski, P.; Specchia, S.; Kotarba, A.; Specchia, V. Pd/Co<sub>3</sub>O<sub>4</sub>-based catalysts prepared by solution combustion synthesis for residual methane oxidation in lean conditions. *Catal. Today* **2015**, *257*, 66–71. [[CrossRef](#)]
19. Lu, N.; Wu, Z.-W.; Lei, L.-J.; Qin, Z.-F.; Zhu, H.-Q.; Luo, L.; Fan, W.-B.; Wang, J.-G. Catalytic combustion of lean methane over a core-shell structured Pd-Co<sub>3</sub>O<sub>4</sub>@SiO<sub>2</sub> catalyst. *Ranliao Huaxue Xuebao* **2015**, *43*, 1120–1127.
20. Wang, Q.; Peng, Y.; Fu, J.; Kyzas, G.Z.; Billah, S.M.R.; An, S. Synthesis, characterization, and catalytic evaluation of Co<sub>3</sub>O<sub>4</sub>/γ-Al<sub>2</sub>O<sub>3</sub> as methane combustion catalysts: Significance of Co species and the redox cycle. *Appl. Catal. B* **2015**, *168–169*, 42–50. [[CrossRef](#)]

21. Wu, Z.; Deng, J.; Liu, Y.; Xie, S.; Jiang, Y.; Zhao, X.; Yang, J.; Arandiyan, H.; Guo, G.; Dai, H. Three-dimensionally ordered mesoporous  $\text{Co}_3\text{O}_4$ -supported Au-Pd alloy nanoparticles: High-performance catalysts for methane combustion. *J. Catal.* **2015**, *332*, 13–24. [CrossRef]
22. Chen, Z.; Wang, S.; Liu, W.; Gao, X.; Gao, D.; Wang, M.; Wang, S. Morphology-dependent performance of  $\text{Co}_3\text{O}_4$  via facile and controllable synthesis for methane combustion. *Appl. Catal. A* **2016**, *525*, 94–102. [CrossRef]
23. Hu, W.; Lan, J.; Guo, Y.; Cao, X.-M.; Hu, P. Origin of Efficient Catalytic Combustion of Methane over  $\text{Co}_3\text{O}_4$ : Active Low-Coordination Lattice Oxygen and Cooperation of Multiple Active Sites. *ACS Catal.* **2016**, *6*, 5508–5519. [CrossRef]
24. Sun, Y.; Liu, J.; Song, J.; Huang, S.; Yang, N.; Zhang, J.; Sun, Y.; Zhu, Y. Exploring the Effect of  $\text{Co}_3\text{O}_4$  Nanocatalysts with Different Dimensional Architectures on Methane Combustion. *ChemCatChem* **2016**, *8*, 540–545. [CrossRef]
25. Wang, F.; Zhang, L.; Xu, L.; Deng, Z.; Shi, W. Low temperature CO oxidation and  $\text{CH}_4$  combustion over  $\text{Co}_3\text{O}_4$  nanosheets. *Fuel* **2017**, *203*, 419–429. [CrossRef]
26. Ercolino, G.; Karimi, S.; Stelmachowski, P.; Specchia, S. Catalytic combustion of residual methane on alumina monoliths and open cell foams coated with Pd/ $\text{Co}_3\text{O}_4$ . *Chem. Eng. J.* **2017**, *326*, 339–349. [CrossRef]
27. Kikuchi, R.; Maeda, S.; Sasaki, K.; Wennerström, S.; Eguchi, K. Low-temperature methane oxidation over oxide-supported Pd catalysts: Inhibitory effect of water vapor. *Appl. Catal. A* **2002**, *232*, 23–28. [CrossRef]
28. Demoulin, O.; Rupprechter, G.; Seunier, I.; Le Clef, B.; Navez, M.; Ruiz, P. Investigation of Parameters Influencing the Activation of a Pd/ $\gamma$ -Alumina Catalyst during Methane Combustion. *J. Phys. Chem. B* **2005**, *109*, 20454–20462. [CrossRef] [PubMed]
29. Kucharczyk, B.; Tylus, W. Effect of washcoat modification with metal oxides on the activity of a monolithic Pd-based catalyst for methane combustion. *Catal. Today* **2008**, *137*, 324–328. [CrossRef]
30. Yang, Z.; Yang, P.; Zhang, L.; Guo, M.; Yan, Y. Investigation of low concentration methane combustion in a fluidized bed with Pd/ $\text{Al}_2\text{O}_3$  as catalytic particles. *RSC Adv.* **2014**, *4*, 59418–59426. [CrossRef]
31. Gholami, R.; Alyani, M.; Smith, K. Deactivation of Pd Catalysts by Water during Low Temperature Methane Oxidation Relevant to Natural Gas Vehicle Converters. *Catalysts* **2015**, *5*, 561–594. [CrossRef]
32. Lin, Y.H.; Yu, S.C. Synthesis and structural features of a flux-grown hematite. *J. Geol. Soc. China* **1999**, *42*, 349–358.
33. Roth, W.L. The magnetic structure of  $\text{Co}_3\text{O}_4$ . *J. Phys. Chem. Solids* **1964**, *25*, 1–10. [CrossRef]
34. Slack, G.A. Crystallography and Domain Walls in Antiferromagnetic NiO Crystals. *J. Appl. Phys.* **1960**, *31*, 1571–1582. [CrossRef]
35. Scherrer, P. Bestimmung der Größe und der inneren Struktur von Kolloidteilchen mittels Röntgenstrahlen. In *Nachrichten von der Gesellschaft der Wissenschaften zu Göttingen, Mathematisch-Physikalische Klasse*; DigiZeitschriften: Göttingen, Germany, 1918; pp. 98–100.
36. Conner, W.C.; Falconer, J.L. Spillover in Heterogeneous Catalysis. *Chem. Rev.* **1995**, *95*, 759–788. [CrossRef]
37. Ciuparu, D.; Perkins, E.; Pfefferle, L. In situ DR-FTIR investigation of surface hydroxyls on  $\gamma$ - $\text{Al}_2\text{O}_3$  supported PdO catalysts during methane combustion. *Appl. Catal. A* **2004**, *263*, 145–153. [CrossRef]
38. Naumkin, A.V.; Kraut-Vass, A.; Gaarenstrom, S.W.; Powell, C.J. NIST X-ray Photoelectron Spectroscopy Database, NIST SRD 20, Version 4.1 (Web Version). Available online: <https://srdata.nist.gov/xps/Default.aspx> (accessed on 13 December 2017).
39. Yin, Y.; Rioux, R.M.; Erdonmez, C.K.; Hughes, S.; Somorjai, G.A.; Alivisatos, A.P. Formation of Hollow Nanocrystals Through the Nanoscale Kirkendall Effect. *Science* **2004**, *304*, 711–714. [CrossRef] [PubMed]
40. Wang, W.; Dahl, M.; Yin, Y. Hollow Nanocrystals through the Nanoscale Kirkendall Effect. *Chem. Mater.* **2013**, *25*, 1179–1189. [CrossRef]

